An experimental and computational investigation of the effects of volumetric boundary conditions on the compressive mechanics of passive skeletal muscle

Anurag J. Vaidya
Department of Biomedical Engineering
Lewisburg, PA 17837

*Benjamin B. Wheatley
Department of Mechanical Engineering
Bucknell University
1 Dent Drive
Lewisburg, PA 17837
b.wheatley@bucknell.edu
570-577-3883

Keywords: finite element, viscoelasticity, hyperelasticity, stiffness, confined compression, unconfined compression

* Corresponding author

Abstract

Computational modeling, such as finite element analysis, is employed in a range of biomechanics specialties, including impact biomechanics and surgical planning. These models rely on accurate material properties for skeletal muscle, which comprises roughly 40% of the human body. Due to surrounding tissues, compressed skeletal muscle *in vivo* likely experiences a semi-confined state. Nearly all previous studies investigating passively compressed muscle at the tissue level have focused on muscle in unconfined compression. The goals of this study were to (1) examine the stiffness and time-dependent material properties of skeletal muscle subjected to both confined and unconfined compression (2) develop a model that captures passive muscle mechanics under both conditions and (3) determine the extent to which different assumptions of volumetric behavior affect model results. Muscle in confined compression exhibited stiffer behavior, agreeing with previous assumptions of near-incompressibility. Stress relaxation was found to be faster under unconfined compression, suggesting there may be different mechanisms that support load these two conditions. Finite element calibration was achieved through nonlinear optimization (normalized root mean square error <6%) and model validation was strong (normalized root mean square error <17%). Comparisons to commonly employed assumptions of bulk behavior showed that a simple one parameter approach does not accurately simulate confined compression. We thus recommend the use of a properly calibrated, nonlinear bulk constitutive model for modeling of skeletal muscle *in vivo*. Future work to determine mechanisms of passive muscle stiffness would enhance the efforts presented here.

1 Introduction

Skeletal muscle comprises approximately 40% of the mass of the human body [1]. Computational modeling of passive skeletal muscle is thus essential to simulations of impact biomechanics [2]–[8], rehabilitation engineering [9], [10], surgical planning [11], [12], and bed sore development [9], [13]. These models rely on accurate material properties for skeletal muscle, which have been shown to be anisotropic [14], [15], time dependent [3]–[5], [16], [17], non-linear [3], [17], and asymmetric in regards to tension and compression [18], [19]. However, the compressive behavior of skeletal muscle is not fully understood, particularly regarding the differences in muscle response to *in vivo* loading conditions [3]–[5], [20].

It is likely that *in vivo* muscle experiences a variation between confined and unconfined volumetric boundary conditions [3]–[5], [21], where semi-confinement is created by tissues surrounding the muscle. Nearly all previous studies investigating passively compressed muscle at the tissue level have focused on muscle in unconfined compression (UC) [3]–[5], [22]–[24], where the sample is free to expand laterally when loaded. One group has investigated muscle under anisotropic semi-confined compression, and the specific confinement was found to affect both muscle structural deformation and mechanical response [14], [15]. Traditionally, muscle has been modelled as a nearly incompressible hyperelastic material [14], [24]–[26]. However, to the best of the authors' knowledge, there have been no investigations of skeletal muscle in fully confined compression (CC), where volumetric strain is applied and the assumption of near incompressibility can be directly tested. This gap in understanding the effects of volumetric boundary conditions (UC and CC) on the compressive properties of skeletal muscle affect the subsequent models derived to predict skeletal muscle and whole body behavior.

The time dependent nature of muscle can be observed in significant stress relaxation following compressive deformation [3]–[5], [16], [17]. Stress relaxation tests have been thus used extensively to characterize the stress-strain and stress-time behavior of the tissue, and are typically accompanied by various viscoelastic modelling approaches [3], [4], [17], [27]–[29]. Inverse finite element methods are effective in determining material properties through parameter optimization to experimental data [27], [30]–[32]. In previous continuum mechanics based modeling of skeletal muscle, the assumption of near incompressibility leads to a decoupling of the volumetric (volume changing) and isochoric (shape changing) responses of the hyperelastic model [23], [33]. We developed a non-linear hyper-viscoelastic finite element model to simulate both UC and CC testing conditions concurrently that was calibrated using inverse finite element analysis through a nonlinear optimization protocol. This model was then used to investigate various assumptions about muscle compressibility, and what the most appropriate modelling approaches may be for passively compressed skeletal muscle.

The goals of this study were to (1) examine the stiffness and time-dependent material properties of skeletal muscle subjected to two boundary conditions (UC and CC) (2) develop a computational model that captures the behavior of muscle subject to these different volumetric boundary conditions and (3) determine the extent to which different assumptions of volumetric behavior affect model results. We hypothesize that the material properties of skeletal muscle differs in confined versus unconfined compression. Since *in vivo* muscle behavior is likely to be semi-confined, we also believe that by considering both conditions we improve the accuracy of finite element models of skeletal muscle.

2 Methods

2.1 Sample Preparation

Whole tibialis anterior (TA) muscles were isolated from seven female porcine hind limbs following sacrifice [14], [15], [23], [24], [26], [34]. Participants did not handle live animals as all tissue was acquired from a local abattoir. Connective tissues and fat were removed from TA using standard dissection instruments. Two sample geometries were identified for experimentation in this study: transverse oriented cuboids for UC and transverse cylindrical plugs for CC. The cuboids (height = 7.2 ± 0.9 mm, cross-sectional area=149.6±25.7 mm^2, n = 15 for fast compression and n = 14 for slow compression) [14] were acquired using scalpels and a custom tissue slicer. Sample height was measured via micrometer and area was calculated through image analysis prior to testing. The cylindrical plugs (height = 7.1 ± 0.6 mm, n = 16 for fast compression and n = 15 for slow compression) were obtained using metal hole punch (ø = 10mm) and scalpels. Since passive skeletal muscle is an incredibly soft tissue, using a larger metal punch ensured that the sample tightly fit into the compression well. Four to five cuboids and cylindrical plugs were excised from each muscle and the samples were not paired between unconfined and confined compression. All samples were taken from muscle midbelly and were kept hydrated by phosphate buffered saline throughout testing [24], [26], [34]. To limit effects of rigor mortis, all testing was completed within eight hours of sacrifice [3]–[5], [17], [29], [35]. Tissue damage was controlled at two points in experimental protocol. Firstly, during dissection, a custom slicer and high-profile histology blades or surgical scalpels were used to cut the sample as few times as possible. Secondly, after each UC and CC tests, the sample was visually checked for damage, and any damaged sample was discarded.

2.2 Experimentation

Custom instrumentation was fabricated to perform UC and CC using a uniaxial tabletop Instron 3366 tensile testing system. A lightweight delrin top and a fixed stainless steel bottom platen were used for UC testing (Figure 1A). An Al2O3 porous plunger (diameter = 6.4 mm, length = 25.5 mm) was used along with an impermeable steel well (diameter = 6.9 mm, depth = 8 mm) for CC (Figure 1B).

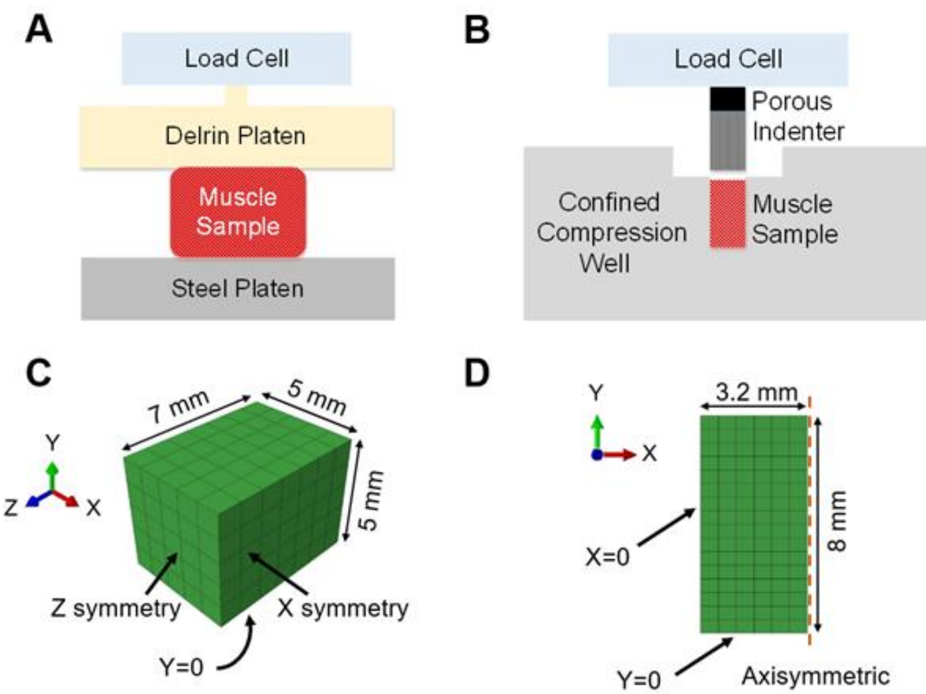

Figure 1: Schematics showing experimental set up for (A) unconfined compression and (B) confined compression. Associated finite element geometry and boundary conditions for (C) unconfined compression and (D) confined compression. Unconfined finite element geometry used quarter symmetry and confined geometry used axisymmetric.

Two stress relaxation testing conditions were employed for both UC and CC conditions: fast and slow compression stress relaxation [5], [29], [36]. All tests were completed under transverse compression to simulate the most common uniaxial physiological loading orientation [15], [22], [23], [34], [37]. For UC, all samples were strained to 40% compressive nominal strain at either 40% s^{-1} (fast compression, n=15) or 5% s^{-1} (slow compression, n=14) [15], [38], [39]. For CC, all samples were strained to 15% compressive nominal strain at either 15% s^{-1} (fast compression, n=16) or 1.5% s^{-1} (slow compression, n=15). All samples were subject to a 400 seconds stress-relaxation hold [4]. Data was acquired by either a 10N or 100N Instron load cell (2350 series) at 100 Hz. Time (seconds), extension (mm), and load (Newtons) were recorded. All model calibration (determination of model parameters) was completed with fast-compression data, while slow-compression data were only used for model validation.

2.3 Data Analysis and Viscoelastic Modelling

First Piola-Kirchhoff (PK) stress P, nominal strain ε, and peak stress were determined through original specimen dimensions (Equation 1, where F is the measured load and A_o is the original specimen cross-sectional area) [17], [28]. Peak modulus ($P_{peak}/\varepsilon_{peak}$) was also calculated. Three relaxation ratios (1-5s, 6-105s, 106-400s) were determined to evaluate the amount of relaxation associated with various relaxation times (Equation 2, where RR is the relaxation ratio and P_i and P_j are the first PK stress at time points i and j) [29]. These three time periods were chosen as they generally characterized “short”, “medium”, and “long” term relaxation for the samples tested in this study, and are similar to time periods previously used for skeletal muscle in tension [29].

$$P = \frac{F}{A_0} \tag{1}$$

$$RR = \frac{P_i - P_j}{P_i} \tag{2}$$

To more finely characterize relaxation behavior, a three term Prony series quasi-linear viscoelastic model (Equations 3-4) was fit to normalized hold phase stress from all testing groups [17], [28], [39]–[41].

$$P(\varepsilon, t) = \int_0^t E(t-\tau)\ \frac{d\varepsilon(\xi)}{d\xi} d\xi \tag{3}$$

$$E(t) = E_0(1 - \sum_{i=1}^{3} E_i \left[1 - \exp\left(-\frac{t}{\tau_i}\right)\right]) \tag{4}$$

Here stress P is calculated from the convolution integral (Equation 3), which includes the Prony series reduced relaxation function $E(t)$, nominal strain ε, and an integration parameter ξ. This includes three relaxation coefficients E_i, three time constants τ_i, and the instantaneous modulus E_0. As the purpose of this analysis was to compare relaxation behavior only, $E_0 = 1$ was fixed and all data were normalized. The model also accounted for the experimental overshoot in strain applied by the Instron during fast compression. Parameter determination was performed in two steps: a Monte Carlo simulation followed by a nonlinear least-squares deterministic optimization (*lsqnonlin* in MATLAB) [27], [28], [30], [42]–[45]. In the Monte Carlo simulation, the six parameters (E_{1-3} and τ_{1-3}) were randomly varied for 100,000 simulations, ensuring $0 < E_1 + E_2 + E_3 < 1$ [30]. The set of parameters minimizing percent error between normalized model and experimental hold stress was used as initial guesses for the deterministic optimization, which optimized percent difference between normalized model and experimental hold stresses. This approach used the global stochastic Monte Carlo method in conjunction with the precision of a local deterministic approach. All modelling was performed in MATLAB (The Mathworks, Inc.).

2.4 Finite Element Modelling

Two finite element models of UC and CC geometries were developed and simulated with an implicit finite element approach in Abaqus/Standard (Dassault Systèmes). (Figure 1C-D). The UC geometry was reduced to a quarter of the sample by symmetry, with 175 first-order 8-node hexahedral elements with a cubic volume of 1 mm^3 (type C3D8RH). This model was compressed by coupling the top surface to a reference node and displacing the node to follow experimental displacement. The reaction force on the reference point was divided by initial area to acquire first Piola-Kirchhoff stress. The CC geometry was reduced to a two-dimensional axisymmetric model of cylinder with 96 first-order 4-node quadrilateral elements with a rectangular area of 3.75 mm^2 (type CAX4RH). A convergence study was performed by doubling and halving the mesh densities, and the model outputs were virtually identical to the outputs of the original models. Displacement was prescribed for top surface and as no lateral expansion occurred, first Piola-Kirchhoff stress was determined directly from model axial stress. Displacements in both fast compression models simulated the slight experimental overshoot applied by the Instron. Four boundary conditions were applied to the UC model to ensure quarter symmetry while leaving exposed faces to expand due to the Poisson effect (Figure 1C). Since very little sample sliding was noticed during pilot testing or experimentation, sliding was not controlled and was not included in any of the models. An axisymmetric rectangular model was developed to simulate the cylindrical CC testing geometry with restricted exterior faces to simulate the impermeable steel well (Figure 1D). Any initial lateral pressure exerted by the walls of the CC well during insertion and prior to loading were small compared to the loading experienced by the sample during tests. Thus, it was deemed appropriate to model the CC well as a fixed boundary with no pre-stress.

A quasi-linear hyper-viscoelastic material formulation was chosen to model the behavior of skeletal muscle subject to both CC and UC [3], [23], [26], [38]. The model utilized a Yeoh form [41] of a polynomial hyperelastic strain energy density function $\Psi(\mathbf{C})$ (Equation 5). The initial shear modulus G_0 and bulk modulus K_0 are given according to the $N = 1$ hyperelastic material parameters (Equation 6) [38], [41].

$$\Psi(\mathbf{C}) = \sum_{i=1}^{3} C_{i0}\,(\bar{I}_1 - 3)^i + \sum_{i=1}^{2} \frac{1}{D_i}(J-1)^{2i} \tag{5}$$

$$G_0 = 2\mathrm{C}_{10},\;\; K_0 = \frac{2}{D_1} \tag{6}$$

Here C_{i0} and D_i are material parameters that characterize the isochoric and volumetric responses, respectively. $\bar{I}_1$ is defined as $\bar{I}_1 = \bar{\lambda}_1 + \bar{\lambda}_2 + \bar{\lambda}_3$ where $\bar{\lambda}_i = J^{-\frac{1}{3}}\lambda_i$ (λ_i are the principle stretches), and J is the volume ratio. Due to the nonlinearity of the stress-strain curves for UC and CC data, three C_{i0} terms and two D_i terms were used. A Prony series viscoelastic model (Equation 7) was applied to the decoupled responses in Equation 4. Here $K(\tau)$ is the time dependent bulk modulus and $G(\tau)$ is the time dependent shear modulus. K_∞ and G_∞ model long-term bulk and shear moduli, respectively. τ_i^K and τ_i^G are time constants ($\tau_1^G = \tau_1^K = 0.05s,\; \tau_2^G = \tau_2^K = 1s,\; \tau_3^G = \tau_3^K = 20s,\; \tau_4^G = \tau_4^K = 400s$) [17], [28], [30], [46]–[48]

$$K(\tau) = K_\infty + \sum_{i=1}^{4} K_i e^{-\frac{\tau}{\tau_i^K}} \qquad G(\tau) = G_\infty + \sum_{i=1}^{4} G_i e^{-\frac{\tau}{\tau_i^G}} \tag{7}$$

The finite element model consisted of thirteen parameters (five hyperelastic, eight viscoelastic). Model calibration (determination of parameters) was again achieved in two steps: a Monte Carlo simulation followed by a nonlinear least-squares deterministic optimization (*lsqnonlin* in MATLAB) [27], [28], [30],

[42]–[45]. For computational efficiency, the Monte Carlo simulation made 5000 random guesses for the eight viscoelastic parameters (all hyperelastic parameters set to 1) and the error function (Equation 8) was used to calculate the weighted difference between normalized model and experimental fast-compression stress relaxation data for both UC and CC models simultaneously. This function assigns greater weight around the peak region where there are fewer time points, thus improving the fit throughout the optimization procedure. The set of bulk-viscoelastic parameters minimizing the CC error and set of shear-viscoelastic parameters minimizing UC error were used as initial guesses for the deterministic optimization. Initial guesses for all hyperelastic parameters were set to a value of one. Following calibration, UC and CC slow-compression data were predicted by this optimized model as a means of validation. Due to the simple and symmetric model geometries in this work, mesh convergence analysis showed virtually no difference in model behavior as a function of element size.

$$error = \sum_{t=0}^{t_{peak}} t * (P_{model} - P_{exp}) + \sum_{t=t_{peak}}^{401} \frac{(P_{model} - P_{exp})}{t} \tag{8}$$

A second set of UC and CC finite element models with the same constitutive formulation were calibrated using only the UC fast compression data. This is to reflect the approach of assuming near-incompressibility with a single-parameter bulk hyperelastic term, as is most common in finite element models of skeletal muscle [23], [25], [33], [49], [50]. The volumetric parameters (D_i) were assumed to be three, four, and five orders of magnitude larger than the isochoric parameters (C_{i0}) to reflect a range of assumptions. The time dependent bulk (K_i) and shear (G_i) moduli were assumed to the same. This model represents the typical approach for finite element modeling of skeletal muscle and was later used to predict the CC fast compression data.

Finally, a semi-confined compression model (SC) was developed by surrounding the quarter-brick UC model with a generic linear elastic material to create a quarter disk (Figure 2A). The outer boundary of this disk was restricted laterally, thus while the whole structure was subject to confined compression, modulating the Young's modulus of this outer material enabled a semi-confined state for the muscle geometry. This modulation then enabled the simulation of a transition from unconfined (Figure to 2B) to confined (Figure 2C) compression during a 40% compressive strain ramp to mimic the UC model strain. As the Young's Modulus of the disk was varied, the SC model stress and volume ratio from the peak were recorded. This parametric analysis was performed for the optimized parameters and parameters acquired from the three models calibrated using UC fast compression data.

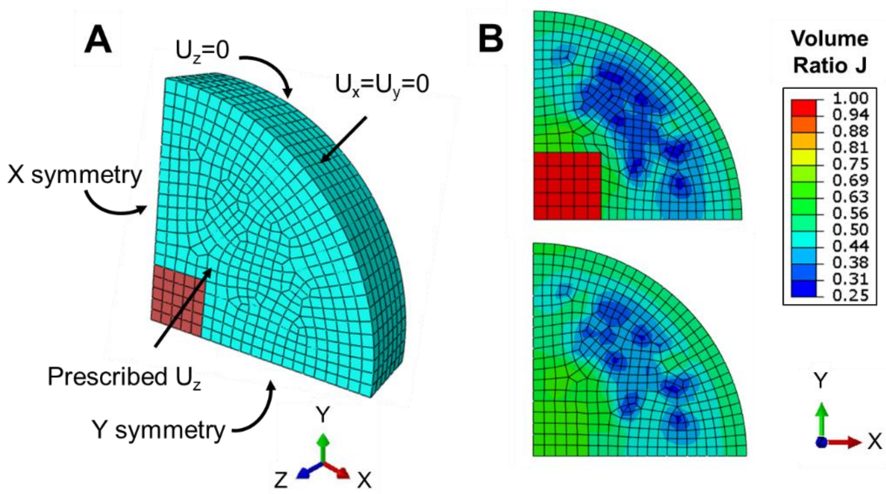

Figure 2: Finite element geometry and boundary conditions of semiconfined compression. The muscle component used the same unconfined quarter brick employing symmetry. The surrounding material completes a quarter-disk of the same height (7 mm) and a radius of 20 mm.

To investigate the variability of the experimental data collected, the finite element model was fit to the upper and lower bounds of the standard deviation curves. In short, the full model optimized parameters were scaled up or down to match experimental data in four additional cases: both UC and CC plus one standard deviation (UC+/CC+), both UC and CC minus one standard deviation (UC-/CC-), and the two remaining cases with one plus standard deviation and one minus standard deviation(UC+/CC- and UC-/CC+). The resulting parameters provide insight into how the variability of the data presented here affect the observed incompressibility of passive skeletal muscle. Specifically, the initial Poisson's ratio ν was determined for each case based on the initial shear and bulk moduli (Equation 9) [51].

$$\nu = \frac{3\frac{K_0}{G_0}-2}{6\frac{K_0}{G_0}+2} \quad (9)$$

2.5 Statistical Analysis

All statistical comparisons between groups were performed using two-sample two-tailed t-tests, with significance set to $p<0.05$. The goodness of fit (GoF) for all fits were evaluated with the goodnessOfFit function in MATLAB (Equation 10) [30]. Here P_i^{mod} and P_i^{exp} are the model and experimental stress values, respectively, at the i^th data point and N is the total number of data points. Fits range from -∞ (worst) to 1 (perfect). The overall percent error, peak stress percent error, and normalized root mean square error (NRMSE) were also determined (Equation 11) [30].

$$GoF = 1 - \sum_{i=1}^{N}\left[\frac{P_i^{mod}-P_i^{exp}}{P_i^{mod}-mean(P_i^{exp})}\right]^2 \quad (10)$$

$$NRMSE = \frac{\sqrt{\sum_{i=1}^{N}(P_i^{mod}-P_i^{exp})^2}}{mean(P^{exp})} \quad (11)$$

3 Results

Despite lower strain levels, muscle in CC exhibited stiffer behavior than muscle in UC in both fast and slow compression. Muscle in CC showed ~1200% higher peak modulus (p-value<0.001) (Figures 3-4) (mean UC fast peak modulus = 0.0524 ± 0.0340 MPa, mean CC fast peak modulus = 1.856 ± 0.908 MPa). Muscle in CC slow compression exhibited a ~860% higher peak stress than muscle in UC slow compression (p-value<0.001) (Figures 3-4) (mean UC slow peak modulus = 0.041 ± 0.020 MPa, mean CC slow peak modulus = 1.058 ± 0.623 MPa).

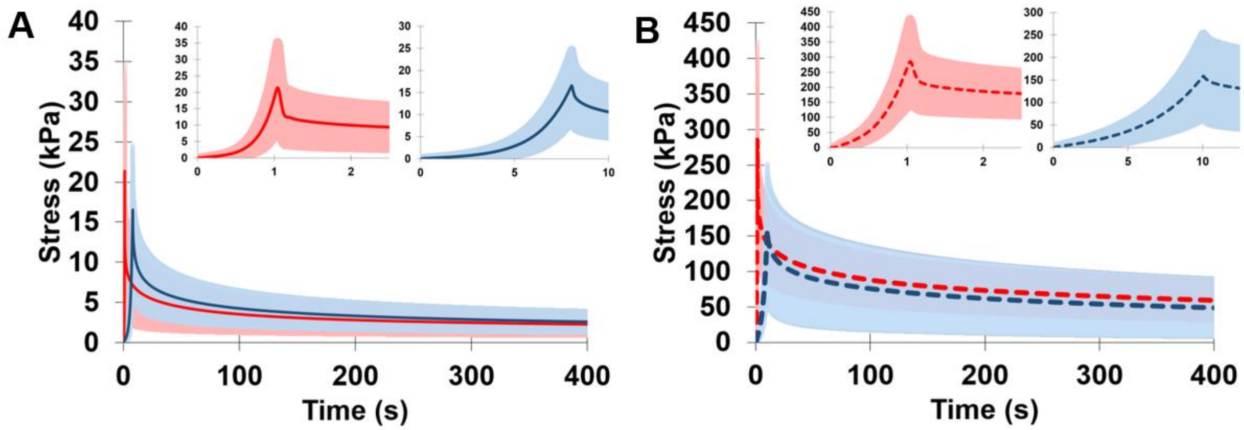

Figure 3: Average experimental stress relaxation curves with standard deviation for (A) unconfined fast (solid red) and slow (solid blue) compression, and (B) confined fast (dashed red) and slow (dashed blue) compression.

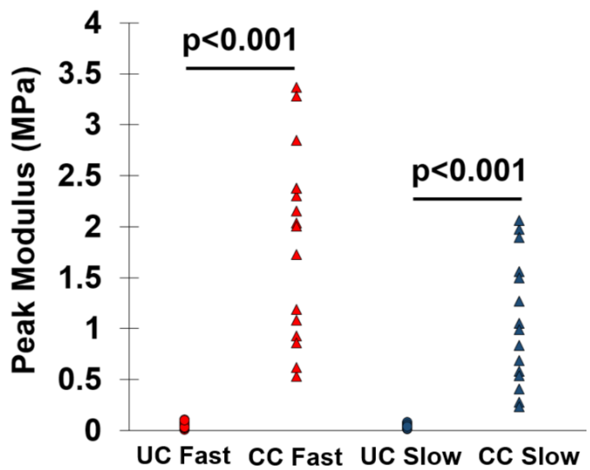

Figure 4: Peak moduli of muscle samples for the four testing conditions and t-test p-values. Unconfined compression is represented by circles and confined compression by triangles.

Muscle in CC and UC fast relaxation showed different relaxation behavior (Figure 5A). The three relaxation ratios (RR1 for 1-5s, RR2 for 6-105s, and RR3 for 106-400s) showed that differences in CC and UC fast compression time dependence was more apparent at the early stage of relaxation. RR1 for UC

(0.648±0.043) was approximately twice RR1 for CC (0.344±0.191) ($p<0.001$). RR2 for UC (0.519±0.076) was larger than RR2 for CC (0.403±0.180) ($p=0.029$), while RR3 was not different ($p=0.521$) (Figure 5B).

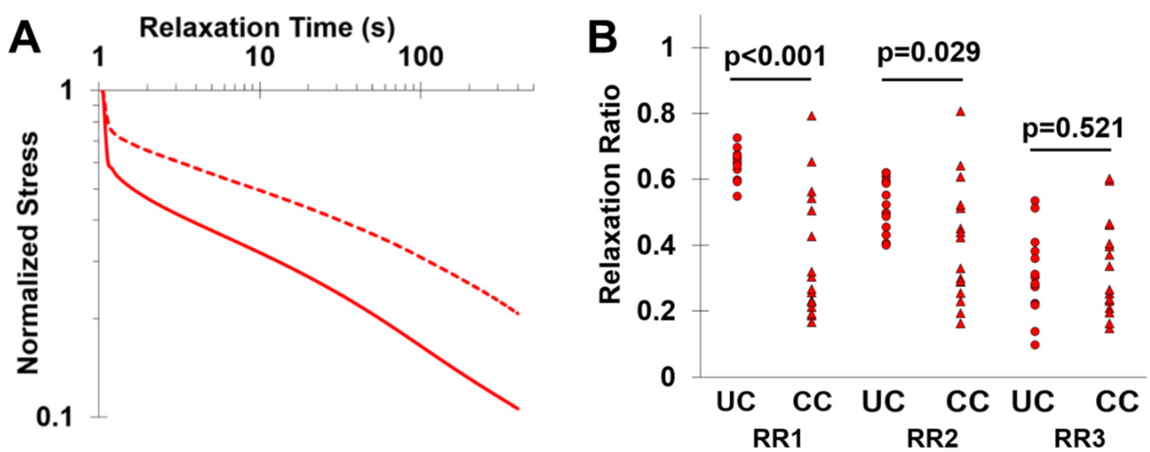

Figure 5: (A) Average normalized experimental stress relaxation curves for the hold phase plotted on logarithmic scales for unconfined (solid red) and confined (dashed red) fast compression. (B) Relaxation ratios RR1-3 for unconfined and confined fast compression data and t-test p-values. Unconfined compression is represented by circles and confined compression by triangles.

The global stochastic Monte Carlo simulation in conjunction with the deterministic optimization yielded excellent fits between the three-term linear Prony series viscoelastic model and normalized experimental stress data (average percent error = 1.06 ± 0.13%, average NRMSE = 0.016 ± 0.002, average GoF = 0.998 ± 0.0002). Comparisons of fast compression viscoelastic parameters showed E_1 for UC (0.902±0.036) was larger than that for CC (0.604±0.192) ($p<0.001$), E_2 for UC (0.043±0.015) was smaller than that for CC (0.103±0.038) ($p<0.001$), and E_3 for UC (0.033±0.019) was smaller than that for CC (0.141±0.078) ($p<0.001$) (Figure 6A). Additionally, τ_1 for UC (0.132±0.029 s) was smaller than that for CC (0.331±0.190 s) ($p<0.001$), τ_2 for UC (7.612 ±1.667 s) was smaller than that for CC (12.751±0.427 s) ($p<0.001$), and τ_3 for UC (96.824±20.134 s) was smaller than that for CC (183.419±90.805 s) ($p<0.001$) (Figure 6B).

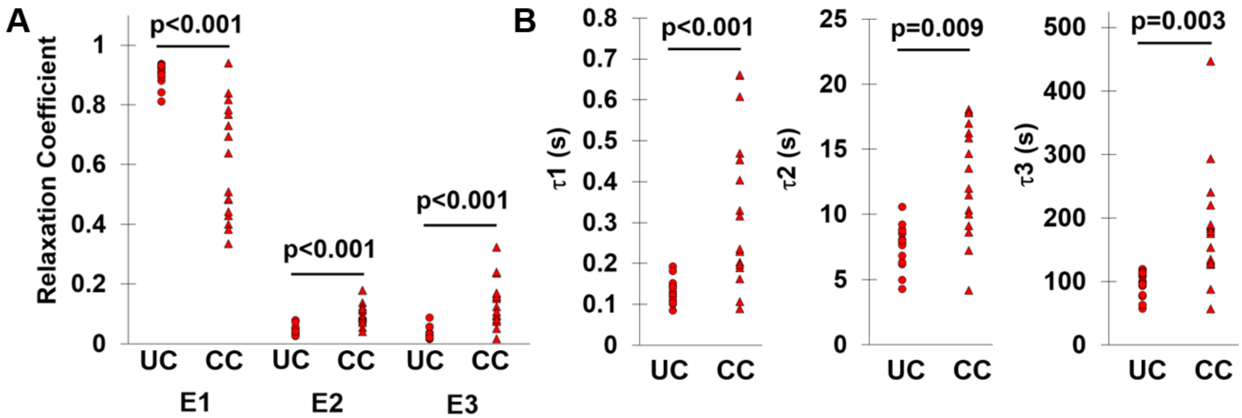

Figure 6: (A) Relaxation parameters E_{1-3} for unconfined and confined fast compression. (B) Time constants τ_{1-3} for unconfined and confined fast compression. Unconfined compression is represented by circles and confined compression by triangles.

The global stochastic Monte Carlo in conjunction with the deterministic optimization again yielded strong concurrent fitting between the finite element model and experimental UC and CC fast data (Table 1) (Figure 7A-B). The initial shear and bulk modulus were calculated using the optimized hyperelastic parameters in Table 2 as 0.0445 kPa and 18.89 kPa, respectively [52]. The model also exhibited very strong predictions for non-linear ramp and relaxation for the slow compression data for both UC and CC (Table 1) (Figure 7C-D).

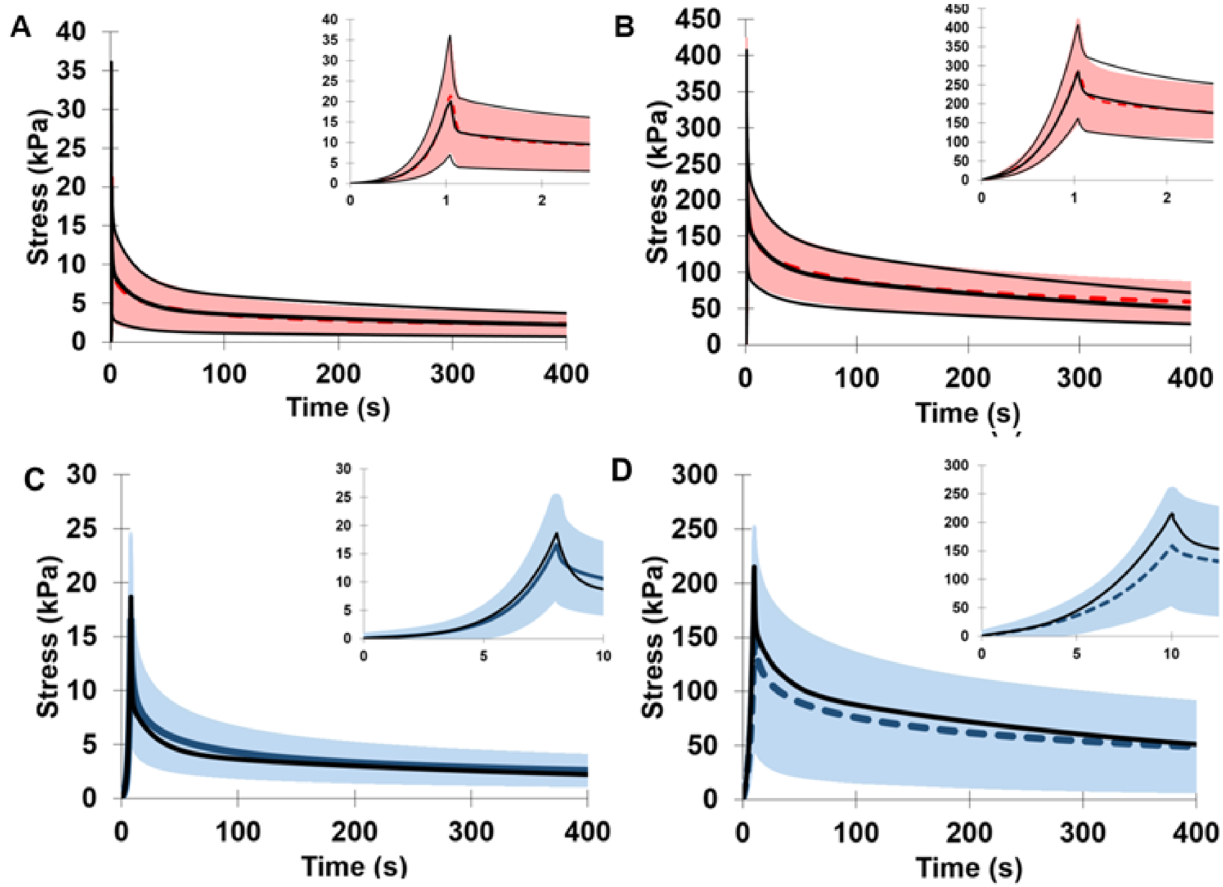

Figure 7: Average fast experimental data with standard deviation, finite element model calibrations, and fits to the standard deviation curves for (A) unconfined compression (experiment in solid red, model in solid black) and (B) confined compression (experiment in dashed red, model in solid black). Average slow experimental data with standard deviation and finite element model predictions for (C) unconfined compression (experiment in solid blue, model in solid black) and (D) confined compression (experiment in dashed blue, model in solid black).

Table 1: Overall percent error, peak error, normalized root mean square error (NRMSE), and goodness of fit (GoF) values for finite element models calibrated to fast unconfined and confined compression data concurrently and validated against slow unconfined and confined compression data concurrently.

Error Type	Model Type	UC	CC
Percent error	**Calibration**	3.6%	5.9%
	Validation	12.1%	14.1%

Peak error	**Calibration**	0.8%	-0.4%
	Validation	11.2%	35.4%
NRMSE	**Calibration**	4.6%	5.6%
	Validation	14.3%	16.8%
GoF	**Calibration**	0.99	0.96
	Validation	0.88	0.64

Table 2: Hyperelastic and viscoelastic parameters of the finite element model calibrated using unconfined and confined fast compression data concurrently.

Parameter Type	Parameter Symbol	Parameter Value
Hyperelastic (MPa)	C_{10}, C_{20}, C_{30}	2.23e-05, 1.28e-04, 2.52e-05
Hyperelastic (MPa^{-1})	D_1, D_2	105.9, 0.839
Shear Coefficients (-)	G_1, G_2, G_3, G_4	0.741, 0.086, 0.093, 0.061
Bulk Coefficients (-)	K_1, K_2, K_3, K_4	0.563, 0.150, 0.108, 0.147

The finite element model with the D_i parameters derived from the C_{i0} and the bulk and shear coefficients equal gave strong fits to the UC data (Table 3). However, these models provided poor predictions for the CC fast data, specifically missing the non-linear ramp, stiffness, and the relaxation behavior (Figure 8A-B). The peak stress was seen to increase rapidly with decreasing volume ratio for the semiconfined (SC) model derived from the full optimized parameters (Figure 8C). However, the peak stresses for the three, four, and five orders of magnitude parameters increased more linearly and were thus comparatively too stiff at low strains or too soft at high strains (Figure 8C-D).

Table 3: Overall percent error, peak error, normalized root mean square error (NRMSE), and goodness of fit (GoF) calibration values for finite element models fit with fast unconfined compression data only.

Error Type	3 orders of magnitude	4 orders of magnitude	5 orders of magnitude
Percent error	5.0%	3.9%	5.1%
Peak error	-9.8%	-0.2%	2.7%
NRMSE	5.8%	4.3%	5.3%
GoF	0.98	0.99	0.98

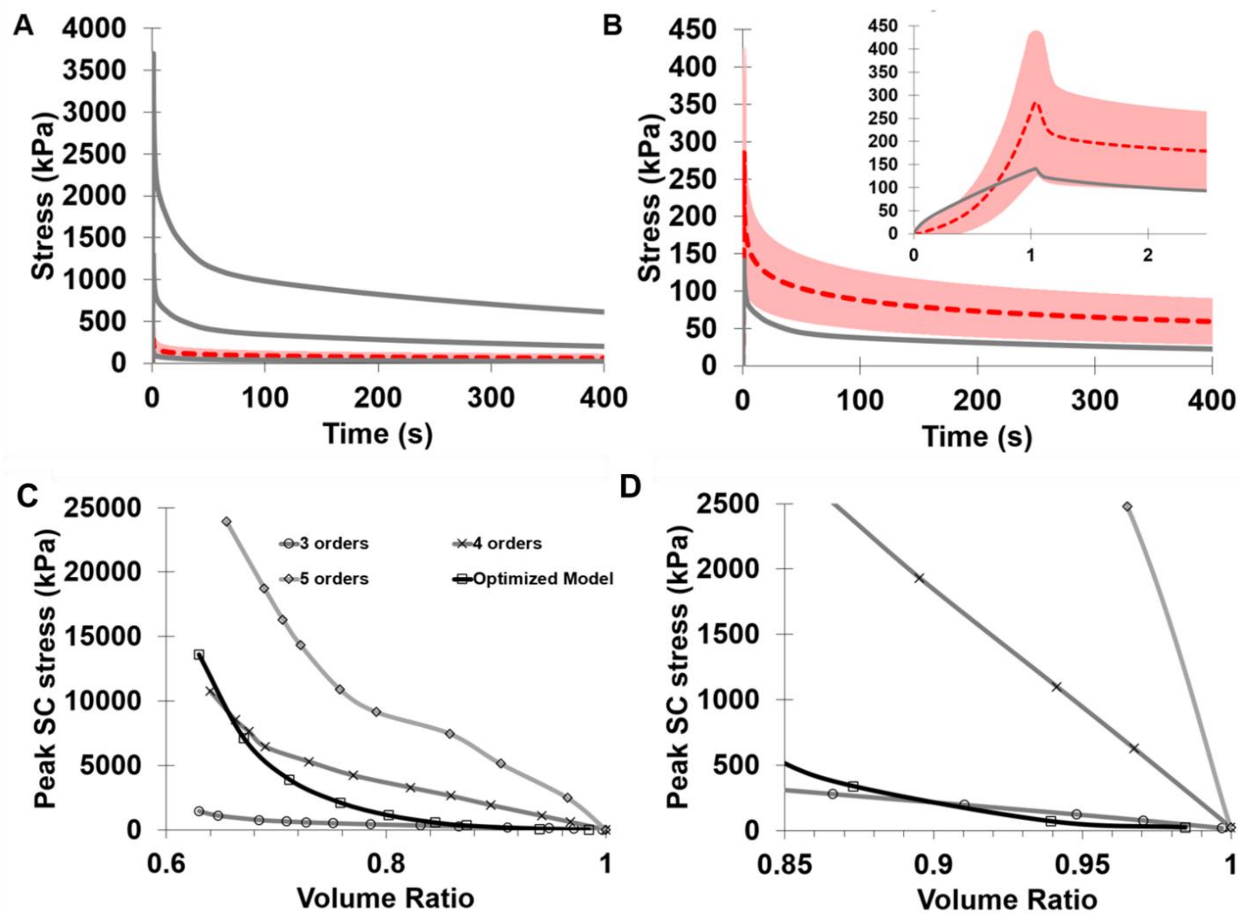

Figure 8: Average confined compression fast experimental data with standard deviation (dashed red) and finite element model predictions (solid gray) for (A) the three, four, and five orders of magnitude predictions, and (B) adjusted y-axis to show only experiment and three orders prediction. (C) Peak stress versus volume ratio for semiconfined compression models calibrated using unconfined data only (gray curves) and semiconfined compression model calibrated using both unconfined and confined compression data (black squares). (D) The same model results presented in (C) shown at lower strain and stress values.

The four sets of bulk and shear moduli calculated from the four new fits (Figure 7 A and B) show the spread in the experimentally found moduli values have only a small effect on initial Poisson's ratio (Table 4). Even with the variability observed and investigated in this study, muscle exhibited nearly-incompressible behavior.

Table 4. Normalized root mean square error (NRMSE), initial bulk and shear moduli, bulk-to-shear modulus ratio, and initial Poisson's Ratio for the additional four fits to the mean experimental data plus or minus standard deviation.

Model Type	**UC NRMSE**	**CC NRMSE**	**Bulk Modulus (kPa)**	**Shear Modulus (kPa)**	**Ratio (Bulk : Shear)**	**Poisson's Ratio**
Mean	4.6%	5.6%	18.89	0.045	423.45	0.499
UC+/CC+	5.4%	6.6%	26.70	0.075	355.64	0.499
UC+/CC-	6.1%	6.2%	10.56	0.014	749.53	0.499
UC-/CC+	8.9%	6.6%	10.56	0.078	135.63	0.496
UC-/CC-	8.8%	6.3%	26.72	0.014	1911.86	0.500

4 Discussion

This study aimed to characterize and compare the stress relaxation behavior of skeletal muscle subject to two volumetric boundary conditions (unconfined compression or UC and confined compression or CC) by comparing stress relaxation data and computational models. We chose to employ both UC and CC conditions as *in vivo* muscle is likely to experience semi-confined compression (SC) where the muscle is partially restricted by surrounding hard and soft tissues. While previous viscoelastic approaches successfully modelled stress relaxation of muscle in UC alone [3], [4], this study simultaneously fit stress relaxation data of muscle in CC and UC, thus providing greater accuracy for the volumetric behavior of skeletal muscle.

4.1 Experimental Findings

Van Loocke et al. found that muscle exhibited a Cauchy stress of ~4 kPa in UC in cross-fiber direction at strain of 30% applied at quasi-static rate of 0.05% s^{-1} [3]. This stress value is comparable to the First Piola-Kirchhoff stress values from UC following relaxation (<5 kPa). Palevski et al. measured the short term and long-term shear modulus of porcine gluteus muscle *in vitro* by rapid indentation tests [53]. They found the shear modulus to be ~700±300 Pa. The hyperelastic finite element model developed in this study yielded a shear modulus of 445 Pa, which agrees well with these previously published data. A later Van Loocke et al. study used a non-linear viscoelastic model and found the shear modulus to be 523 Pa, which is also in close agreement with the shear modulus found in this study [4].

The linear viscoelastic model shows that there is approximately 97% relaxation of muscle instantaneous modulus associated relaxation (Figure 6) for UC. This finding agrees with the findings of Van Loocke et al., whose viscoelastic model showed that muscle experiences about 80% relaxation in first 100 seconds of the hold phase of stress relaxation tests. Wheatley et al. also found that muscle exhibits up to 99% relaxation in UC at long relaxation times, and also found muscle exhibits initial relaxation of ~75%, which is consistent with what our viscoelastic model shows (Figure 6) [28]. On the other hand, muscle in CC shows nearly half of initial relaxation that muscle in UC exhibited (Figure 5). This is supported by statistical comparisons of viscoelastic parameters (Figure 6). In all, the time dependent behavior of skeletal muscle has been shown to depend on the loading condition.

Muscle has been known to be ~70-80% incompressible fluid [54] and some studies suggest this fluid plays a significant role in the mechanical properties of the tissue [55]–[58]. In UC, when muscle is compressed, fluid is free to redistribute within the tissue while maintaining a nearly constant volume and exude from the sample from the pores on the lateral sides. Thus, it is unlikely to directly bear a significant portion of the load, leaving solid muscle constituents such as the extracellular matrix and myofibrils to perhaps resist compression directly. When load is applied to muscle in CC, the fluid cannot escape laterally, and must flow through the porous indenter. Fluid could then be retained in interstitial and intracellular space, thus pressurizing and supporting a greater load than in UC. Since fluid is incompressible, this effect can lead to drastic differences in observed stiffness between UC and CC such as those observed here. This fluid pressurization may also contribute the differences in relaxation behavior between UC and CC, as muscle has been shown to have a non-negligible permeability [57]. However, this hypothesis remains untested and future work should be completed to directly investigate fluid pressurization's effect on viscoelastic behavior of muscle in different loading conditions.

Two sample geometries were identified for experimentation in this study: transverse oriented cuboids for UC and transverse cylindrical plugs for CC. To minimize tissue damage, high profile histology blades and surgical scalpels were used for dissection. These geometries, in accordance with previous literature [59], [60] were used due to the constraints from the experimental apparatus used (Figure 1 A and B). Specifically, the differences in tissue stiffness and required boundary conditions based on testing condition made using a single sample geometry between tests unreasonable. While previous work has shown that sample size can affect the observed compressive modulus of passive skeletal muscle [61] sample size and dimension are not likely to explain the major differences in compressive stiffness observed in this study. Additionally, the size of muscle fibers (~50-100 μm) relative to the sample size used here (multiple mm) suggest that the specimens used in this study are representative of bulk muscle tissue.

While the stress-time data and standard deviation presented here shows that not all samples exhibited identical passive material properties, this is not uncommon for biological soft tissues and in particular skeletal muscle [3], [4], [62]. These differences are often explained by natural variability of structure and content of constituents such as collagen in the extracellular matrix, fiber/fascicle size and organization, and fluid content from animal to animal and muscle to muscle. Despite the fact that clear and consistent structure-function mechanisms in passive skeletal muscle are not fully understood, both the extracellular matrix and muscle fibers are involved in passive load transmission in skeletal muscle [63]–[65]. Other sources of variability may be tissue hydration, although all samples were stored soaked in phosphate buffered saline prior to testing to limit this effect.

One limitation of this work is that muscle samples in UC and CC were compressed to different strain levels. The strain levels of 40% in UC and 15% in CC ensured that enough load was applied to each sample without damaging the samples. These strain levels were determined through extensive pilot stress-relaxation testing to investigate strain level and tissue damage. Due to the highly soft nature of passive skeletal muscle under unconfined compression and the relatively stiff response in confined compression, these two strain levels gave more comparable data than similar strain levels would. As muscle has been shown be nonlinearly viscoelastic in unconfined compression, the differences in relaxation behavior may vary somewhat with strain. However, the major differences in tissue stiffness between testing conditions suggest different mechanisms that support load under UC and CC. Additionally, the effectiveness of bulk and shear Prony series viscoelastic terms employed in this study further support the notion of different mechanisms driving the stiffness and time dependent responses in UC and CC. Future work to test muscle in UC and CC at different strain levels would further clarify how relaxation behavior depends on strain level under these conditions.

4.2 Model Findings

Two modeling approaches were used in this study: an analytical linear Prony series viscoelastic model and an uncoupled Yeoh/Prony hyper-viscoelastic model. Both of these approaches had a similar two-step optimization method, but each model served a different purpose. The relatively simple viscoelastic analytical model generated sets of parameters for each individual sample that could be used to compare relaxation behavior of muscle between unconfined and confined compression. In comparison, the hyper-viscoelastic finite element model was developed to concurrently characterize the behavior of both testing conditions. Together, these two modeling approaches enabled statistical comparison of testing conditions as well as comprehensive characterization of tissue stress relaxation behavior. The finite element model was calibrated using the fast compression data and used to predict the slow compression data as the fast data encompasses a more comprehensive time dependent data set; this is also a common practice in viscoelastic modelling [4], [28]. Moreover, the current study aimed to characterize the larger differences between the testing conditions and not the effect of more specific factors like strain rate, which could be investigated in future studies.

Blemker et al. used a decoupled strain energy formulation to model the biceps branchii in which the volumetric or bulk parameter is assumed to be five orders of magnitude larger than the isochoric or shear parameters [33]. Similarly, Calvo et al. and Grasa et al. take the only volumetric parameter to be between two and three orders of magnitude larger than the isochoric parameters [25], [66]. In this study we collect volumetric compression data (CC) and span the assumptions made by Blemker et al. and Calvo et al to predict the CC data. The predictions are very poor (Figure 8), showing that this simple assumption is not appropriate for representing the nonlinear stress-strain behavior under highly confined compression. We present a finite element model in which the volumetric and isochoric responses are concurrently optimized. Our models still agree that muscle is what would generally be considered to be nearly-incompressible (initial shear modulus of muscle is ~3 orders of magnitude smaller than initial bulk modulus), but that the volumetric response is nonlinear as shown by the strong predictions of a two-term volumetric function (Figure 7). We thus recommend using a higher-order volumetric term to better characterize compressed muscle.

We believe that *in vivo* muscle experiences loading that is most similar to semi-confined compression. This loading could vary between conditions that approach unconfined or confined compression among different muscles in the body, or even in different regions on the same muscle. This is supported by previous magnetic resonance imaging of passively stretched human tibialis anterior that observed volumetric strains as high as 20% in one region and nearly 0% in another [67]. The three models representing literature methods and the model that we concurrently optimized using UC and CC data provide very different results for semi-confinement, particularly regarding nonlinearity (Figure 8B). This may be a concern as passive stiffness nonlinearity could act as a mechanism to prevent damage of bone and other tissues during high impact loads *in vivo*. Additionally, the use of a single-term volumetric formulation is likely to be either too stiff at low volumetric strains or too soft at high volumetric strains.

The study presents a finite element model that can concurrently characterize the unconfined and confined compression conditions. The modeling and optimization approach employed here fit thirteen hyper-viscoelastic parameters. This number of parameters were used because (1) the ramp phase for both unconfined and confined compression are highly non-linear (2) muscle specimens relaxed for a four hundred seconds following compresison at a relatively fast rate (up to 40%/sec), thus enacting a wide range of time dependence. Future work could reduce the number of optimized or varied parameters by locking

Prony terms or coupling terms together similar to previous work [30]. Alternatively, the model provides strong predictions and future efforts could combine direction-dependent, contractile, and tensile mechanics as well to create a more comprehensive model. It has previously been shown that fitting models to average experimental data yields different parameters than fitting model individually to tests and then averaging the parameters [68]. Since goal of the study was to characterize the broader differences between the testing conditions, the authors found it appropriate to only fit the models to averaged data and acquire one set of parameters.

One limitation of the finite element model provided in this study is that it cannot capture the comprehensive properties exhibited by passive skeletal muscle such as tension-compression asymmetry, anisotropy, and contractile properties. It is generally assumed, however, that skeletal muscle is primarily compressed in the transverse direction *in vivo,* thus this is the direction of importance when considering *in vivo* muscle deformation. A comprehensive model is likely to have quite a large number of parameters, thus increasing the model complexity. However, previous studies [30] have explored how parameter coupling can reduce the number of parameters in a model while still utilizing nonlinear optimization and statistical interpretation of model results. In the future, this approach could be employed to implement a model that not only characterizes differences between muscle in unconfined and confined compression but also has other established properties of skeletal muscle. We also chose not to use a biphasic or poroelastic constitutive approach in this work because viscoelasticity what is commonly used to characterize skeletal muscle stress relaxation and is a computationally efficient and stable approach to modeling time dependence. Fluid pressurization, however, requires the solution of an additional condition (either pressure equilibrium or conservation of mass of the fluid) and is more unstable at high strain rates. Future studies exploring the mechanisms involved in tension and compression and could employ mechanistic anisotropic models that include components such as tension only fibers and saturating fluid. This type of a model would be greatly beneficial to the field of passive muscle mechanics.

5 Conclusion

In all, the study found that muscle in CC exhibits stiffer compressive behavior despite lower strains and muscle in UC exhibits greater and faster relaxation. This study also showed that concurrently fitting isochoric and volumetric hyper-viscoelastic parameters with these data improves model predictions, and is recommended for cases where semi-confinement is likely. Future work to better understand the mechanisms of force transmission in compressed skeletal muscle would greatly benefit the field.

6 Acknowledgements and Conflicts of Interest

The authors would like to thank the Program for Undergraduate Research (PUR) at Bucknell University (Lewisburg, PA) for funding. Authors have no conflicts of interest to report.

7 References

[1] I. Janssen, S. B. Heymsfield, Z. M. Wang, and R. Ross, "Skeletal muscle mass and distribution in 468 men and women aged 18-88 yr.," *J. Appl. Physiol.*, vol. 89, no. 1, pp. 81–8, Jul. 2000.

[2] K. L. Troyer and C. M. Puttlitz, "Nonlinear viscoelasticty plays an essential role in the functional behavior of spinal ligaments.," *J. Biomech.*, vol. 45, no. 4, pp. 684–91, Feb. 2012.

[3] M. Van Loocke, C. G. Lyons, and C. K. Simms, "A validated model of passive muscle in compression," *J. Biomech.*, vol. 39, no. 16, pp. 2999–3009, Jan. 2006.

[4] M. Van Loocke, C. G. Lyons, and C. K. Simms, "Viscoelastic properties of passive skeletal muscle in compression: Stress-relaxation behaviour and constitutive modelling," *J. Biomech.*, vol. 41, no. 7, pp. 1555–1566, Jan. 2008.

[5] M. Van Loocke, C. K. Simms, and C. G. Lyons, "Viscoelastic properties of passive skeletal muscle in compression-Cyclic behaviour," *J. Biomech.*, vol. 42, no. 8, pp. 1038–1048, May 2009.

[6] L. van Rooij *et al.*, "The development, validation and application of a finite element upper extremity model subjected to air bag loading.," *Stapp Car Crash J.*, vol. 47, pp. 55–78, Oct. 2003.

[7] M. M. Verver, J. van Hoof, C. W. J. Oomens, J. S. H. M. Wismans, and F. P. T. Baaijens, "A finite element model of the human buttocks for prediction of seat pressure distributions.," *Comput. Methods Biomech. Biomed. Engin.*, vol. 7, no. 4, pp. 193–203, Aug. 2004.

[8] E. E. Ward, M. Kleinberger, A. M. Lennon, and J. C. Roberts, "Modeling the Effects of Blast on the Human Thorax Using High Strain Rate Viscoelastic Properties of Human Tissue," in *IUTAM Symposium on Impact Biomechanics: From Fundamental Insights to Applications*, Berlin/Heidelberg: Springer-Verlag, 2005, pp. 17–24.

[9] E. Linder-Ganz, N. Shabshin, Y. Itzchak, and A. Gefen, "Assessment of mechanical conditions in sub-dermal tissues during sitting: A combined experimental-MRI and finite element approach," *J. Biomech.*, vol. 40, no. 7, pp. 1443–1454, Jan. 2007.

[10] A. F. Mak, M. Zhang, and D. A. Boone, "State-of-the-art research in lower-limb prosthetic biomechanics-socket interface: a review.," *J. Rehabil. Res. Dev.*, vol. 38, no. 2, pp. 161–74, 2001.

[11] J. M. Guccione, S. M. Moonly, A. W. Wallace, and M. B. Ratcliffe, "Residual stress produced by ventricular volume reduction surgery has little effect on ventricular function and mechanics: A finite element model study," *J. Thorac. Cardiovasc. Surg.*, vol. 122, no. 3, pp. 592–599, Sep. 2001.

[12] E. Keeve, S. Girod, R. Kikinis, and B. Girod, "Deformable modeling of facial tissue for craniofacial surgery simulation," *Comput. Aided Surg.*, vol. 3, no. 5, pp. 228–238, 1998.

[13] A. Gefen, N. Gefen, E. Linder-Ganz, and S. S. Margulies, "In Vivo Muscle Stiffening Under Bone Compression Promotes Deep Pressure Sores," *J. Biomech. Eng.*, vol. 127, no. 3, p. 512, 2005.

[14] M. Böl, A. E. Ehret, K. Leichsenring, C. Weichert, and R. Kruse, "On the anisotropy of skeletal muscle tissue under compression.," *Acta Biomater.*, vol. 10, no. 7, pp. 3225–34, Jul. 2014.

[15] M. Böl, K. Leichsenring, M. Ernst, and A. E. Ehret, "Long-term mechanical behaviour of skeletal muscle tissue in semi-confined compression experiments," *J. Mech. Behav. Biomed. Mater.*, vol. 63, pp. 115–124, Oct. 2016.

[16] E. M. H. Bosboom, M. K. C. Hesselink, C. W. J. Oomens, C. V. C. Bouten, M. R. Drost, and F. P. T. Baaijens, "Passive transverse mechanical properties of skeletal muscle under in vivo compression," *J. Biomech.*, vol. 34, no. 10, pp. 1365–1368, Oct. 2001.

[17] B. B. Wheatley, D. A. Morrow, G. M. Odegard, K. R. Kaufman, and T. L. Haut Donahue, "Skeletal muscle tensile strain dependence: Hyperviscoelastic nonlinearity," *J. Mech. Behav. Biomed. Mater.*, vol. 53, pp. 445–454, Jan. 2016.

[18] M. Latorre, M. Mohammadkhah, C. K. Simms, and F. J. Montáns, "A continuum model for tension-compression asymmetry in skeletal muscle," *J. Mech. Behav. Biomed. Mater.*, vol. 77, no. June 2017, pp. 455–460, Jan. 2018.

[19] K. M. Moerman, C. K. Simms, and T. Nagel, "Control of tension–compression asymmetry in Ogden hyperelasticity with application to soft tissue modelling," *J. Mech. Behav. Biomed. Mater.*, vol. 56, pp. 218–228, Mar. 2016.

[20] M. Mohammadkhah, P. Murphy, and C. K. Simms, "The in vitro passive elastic response of chicken pectoralis muscle to applied tensile and compressive deformation," *J. Mech. Behav. Biomed. Mater.*, vol. 62, pp. 468–480, Sep. 2016.

[21] Y. Zheng, A. F. Mak, and B. Lue, "Objective assessment of limb tissue elasticity:

development of a manual indentation procedure.," *J. Rehabil. Res. Dev.*, vol. 36, no. 2, pp. 71–85, 1999.

[22] T. Siebert *et al.*, "Three-Dimensional Muscle Architecture and Comprehensive Dynamic Properties of Rabbit Gastrocnemius, Plantaris and Soleus: Input for Simulation Studies.," *PLoS One*, vol. 10, no. 6, p. e0130985, Jan. 2015.

[23] M. Böl, R. Kruse, A. E. Ehret, K. Leichsenring, and T. Siebert, "Compressive properties of passive skeletal muscle—The impact of precise sample geometry on parameter identification in inverse finite element analysis," *J. Biomech.*, vol. 45, no. 15, pp. 2673–2679, Oct. 2012.

[24] R. Pietsch *et al.*, "Anisotropic compressive properties of passive porcine muscle tissue.," *J. Biomech. Eng.*, vol. 136, no. 11, p. 111003, Nov. 2014.

[25] M. Böl, R. Iyer, J. Dittmann, M. Garcés-Schröder, and A. Dietzel, "Investigating the passive mechanical behaviour of skeletal muscle fibres: Micromechanical experiments and Bayesian hierarchical modelling," *Acta Biomater.*, May 2019.

[26] B. Calvo *et al.*, "Passive nonlinear elastic behaviour of skeletal muscle: experimental results and model formulation.," *J. Biomech.*, vol. 43, no. 2, pp. 318–25, Jan. 2010.

[27] M. Takaza, K. M. Moerman, J. Gindre, G. Lyons, and C. K. Simms, "The anisotropic mechanical behaviour of passive skeletal muscle tissue subjected to large tensile strain," *J. Mech. Behav. Biomed. Mater.*, vol. 17, pp. 209–220, Jan. 2012.

[28] F. Lei and A. Z. Szeri, "Inverse analysis of constitutive models: Biological soft tissues," *J. Biomech.*, vol. 40, no. 4, pp. 936–940, Jan. 2007.

[29] B. B. Wheatley, R. B. Pietsch, T. L. Haut Donahue, and L. N. Williams, "Fully non-linear hyper-viscoelastic modeling of skeletal muscle in compression.," *Comput. Methods Biomech. Biomed. Engin.*, vol. 19, no. 11, pp. 1181–9, Dec. 2016.

[30] B. B. Wheatley, G. M. Odegard, K. R. Kaufman, and T. L. H. Donahue, "How does tissue preparation affect skeletal muscle transverse isotropy?," *J. Biomech.*, vol. 49, no. 13, pp. 3056–3060, Sep. 2016.

[31] B. B. Wheatley, K. M. Fischenich, K. D. Button, R. C. Haut, and T. L. Haut Donahue, "An optimized transversely isotropic, hyper-poro-viscoelastic finite element model of the meniscus to evaluate mechanical degradation following traumatic loading," *J. Biomech.*, vol. 48, no. 8, pp. 1454–1460, Jun. 2015.

[32] R. . Korhonen *et al.*, "Importance of the superficial tissue layer for the indentation stiffness of articular cartilage," *Med. Eng. Phys.*, vol. 24, no. 2, pp. 99–108, Mar. 2002.

[33] M. A. LeRoux and L. A. Setton, "Experimental and biphasic FEM determinations of the

material properties and hydraulic permeability of the meniscus in tension.," *J. Biomech. Eng.*, vol. 124, no. 3, pp. 315–21, Jun. 2002.

[34] S. S. Blemker, P. M. Pinsky, and S. L. Delp, "A 3D model of muscle reveals the causes of nonuniform strains in the biceps brachii.," *J. Biomech.*, vol. 38, no. 4, pp. 657–65, Apr. 2005.

[35] T. A. Krouskop, A. L. Muilenberg, D. R. Doughtery, and D. J. Winningham, "Computer-aided design of a prosthetic socket for an above-knee amputee.," *J. Rehabil. Res. Dev.*, vol. 24, no. 2, pp. 31–8, Oct. 1987.

[36] C. Van Sligtenhorst, D. S. Cronin, and G. Wayne Brodland, "High strain rate compressive properties of bovine muscle tissue determined using a split Hopkinson bar apparatus," *J. Biomech.*, vol. 39, no. 10, pp. 1852–1858, Jan. 2006.

[37] T. Siebert, O. Till, N. Stutzig, M. Günther, and R. Blickhan, "Muscle force depends on the amount of transversal muscle loading.," *J. Biomech.*, vol. 47, no. 8, pp. 1822–8, Jun. 2014.

[38] A. Chawla, S. Mukherjee, and B. Karthikeyan, "Characterization of human passive muscles for impact loads using genetic algorithm and inverse finite element methods," *Biomech. Model. Mechanobiol.*, vol. 8, no. 1, pp. 67–76, Feb. 2009.

[39] B. Song, W. Chen, Y. Ge, and T. Weerasooriya, "Dynamic and quasi-static compressive response of porcine muscle," *J. Biomech.*, vol. 40, no. 13, pp. 2999–3005, Jan. 2007.

[40] P. Aimedieu, D. Mitton, J. P. Faure, L. Denninger, and F. Lavaste, "Dynamic stiffness and damping of porcine muscle specimens," *Med. Eng. Phys.*, vol. 25, no. 9, pp. 795–799, Nov. 2003.

[41] Y. Zheng, A. F. Mak, and B. Lue, "Objective assessment of limb tissue elasticity: development of a manual indentation procedure.," *J. Rehabil. Res. Dev.*, vol. 36, no. 2, pp. 71–85, Apr. 1999.

[42] G. A. Holzapfel, "Biomechanics of soft tissues," *Handb. Mater. Benahior Model. Acad. Press. Waltham, Masschuetts*, pp. 1049–20163, 2001.

[43] M. Kauer, V. Vuskovic, J. Dual, G. Szekely, and M. Bajka, "Inverse finite element characterization of soft tissues," *Med. Image Anal.*, vol. 6, no. 3, pp. 275–287, Sep. 2002.

[44] J. Kim and M. A. Srinivasan, "Characterization of viscoelastic soft tissue properties from in vivo animal experiments and inverse FE parameter estimation.," *Med. Image Comput. Comput. Assist. Interv.*, vol. 8, no. Pt 2, pp. 599–606, 2005.

[45] P. A. L. S. Martins, R. M. Natal Jorge, and A. J. M. Ferreira, "A Comparative Study of Several Material Models for Prediction of Hyperelastic Properties: Application to Silicone-Rubber and Soft Tissues," *Strain*, vol. 42, no. 3, pp. 135–147, Aug. 2006.

[46] S. R. Lucas *et al.*, “Viscoelastic properties of the cervical spinal ligaments under fast strain-rate deformations.,” *Acta Biomater.*, vol. 4, no. 1, pp. 117–25, Jan. 2008.

[47] K. L. Troyer and C. M. Puttlitz, “Human cervical spine ligaments exhibit fully nonlinear viscoelastic behavior,” *Acta Biomater.*, vol. 7, no. 2, pp. 700–709, Feb. 2011.

[48] K. L. Troyer and C. M. Puttlilz, “Nonlinear viscoelasticity plays an essential role in the function bahevior of spinal ligaments,” *J. Biomech.*, vol. 45, pp. 684–691, 2012.

[49] B. Calvo *et al.*, “On modelling damage process in vaginal tissue,” *J. Biomech.*, vol. 42, no. 5, pp. 642–651, Mar. 2009.

[50] “Modeling Skeletal Muscle Stress and Intramuscular Pressure: A Whole Muscle Active–Passive Approach,” *J. Biomech. Eng.*, vol. 140, no. 8, p. 081006, Aug. 2018.

[51] Dassault Systèmes, *Abaqus Theory Manual*. Providence, RI, USA, 2012.

[52] A. Palevski, I. Glaich, S. Portnoy, E. Linder-Ganz, and A. Gefen, “Stress relaxation of porcine gluteus muscle subjected to sudden transverse deformation as related to pressure sore modeling.,” *J. Biomech. Eng.*, vol. 128, no. 5, pp. 782–7, Oct. 2006.

[53] G. Sjøgaard and B. Saltin, “Extra- and intracellular water spaces in muscles of man at rest and with dynamic exercise.,” *Am. J. Physiol.*, vol. 243, no. 3, pp. R271-80, Sep. 1982.

[54] J. Gindre, M. Takaza, K. M. Moerman, and C. K. Simms, “A structural model of passive skeletal muscle shows two reinforcement processes in resisting deformation.,” *J. Mech. Behav. Biomed. Mater.*, vol. 22, pp. 84–94, Jun. 2013.

[55] D. A. Sleboda and T. J. Roberts, “Incompressible fluid plays a mechanical role in the development of passive muscle tension,” *Biol. Lett.*, vol. 13, no. 1, 2017.

[56] B. B. Wheatley, G. M. Odegard, K. R. Kaufman, and T. L. Haut Donahue, “A case for poroelasticity in skeletal muscle finite element analysis: experiment and modeling.,” *Comput. Methods Biomech. Biomed. Engin.*, vol. 20, no. 6, pp. 598–601, May 2017.

[57] M. Yang and L. A. Taber, “The possible role of poroelasticity in the apparent viscoelastic behavior of passive cardiac muscle.,” *J. Biomech.*, vol. 24, no. 7, pp. 587–97, Jan. 1991.

[58] J. Grasa, A. Ramírez, R. Osta, M. J. Muñoz, F. Soteras, and B. Calvo, “A 3D active-passive numerical skeletal muscle model incorporating initial tissue strains. Validation with experimental results on rat tibialis anterior muscle,” *Biomech. Model. Mechanobiol.*, vol. 10, no. 5, pp. 779–787, Oct. 2011.

[59] E. R. Jensen, D. A. Morrow, J. P. Felmlee, N. S. Murthy, and K. R. Kaufman, “Characterization of three dimensional volumetric strain distribution during passive tension of the human tibialis anterior using Cine Phase Contrast MRI,” *J. Biomech.*, vol.

49, no. 14, pp. 3430–3436, Oct. 2016.